Article

Electrical Prospecting of Gold Mineralization in Exhalites of the Digo-Digo VMS Occurrence, Central Brazil

Pedro Augusto Costa do Amaral [1], Welitom Rodrigues Borges [1,*], Catarina Labouré Bemfica Toledo [1], Adalene Moreira Silva [1], Hygor Viana de Godoy [1] and Marcelo Henrique Leão Santos [2]

[1] Institute of Geosciences, University of Brasilia (UnB), Darcy Ribeiro Campus, Brasília 70910-900, DF, Brazil; pedro.amaral.unb@gmail.com (P.A.C.d.A.); catarinatoledo@unb.br (C.L.B.T.); adalene@unb.br (A.M.S.); hygorv@gmail.com (H.V.d.G.)

[2] Faculty of Planaltina, University of Brasilia (UnB), Planaltina 73345-010, DF, Brazil; marcelo.leao@unb.br

* Correspondence: welitom@unb.br; Tel.: +55-619-9646-9090

Abstract: The greenstone belts of the Crixás-Goiás Domain are economically important due to significant epigenetic gold deposits and the potential for under-researched syngenetic deposits. The gold occurrences associated with the volcanogenic massive sulfide (VMS) deposits in the region are documented only in the volcanoclastic rocks of the Digo-Digo Formation, Serra de Santa Rita greenstone belt. The objective of this work is to discuss the efficiency of the induced polarization methods in the time and frequency domains for differentiating and identifying potentially mineralized zones in the exhalites associated with the VMS-type gold of the Digo-Digo Formation. Data were acquired using a multielectrode resistivity meter with the dipole–dipole array and 10 m spacing between electrodes, as well as different current injection times (250, 1000, and 2000 ms). After the electrical data processing and inversion, the sections were integrated into ternary red-green-blue and cyan-magenta-yellow models to highlight areas of high chargeability, low resistivity, and high metal factor (frequency domain) and, thus, map the higher potential zones to host polarizable metallic minerals. The geological–geophysical model elaborated from the correlation of electrical and surface geological data allowed us to identify four anomalous areas related to potential mineralized zones. The geological data confirm that two targets are associated with the geological contacts between metamafic and intermediate metavolcanic units and the exhalative horizon. One of the targets coincides with a sulfide-rich exhalative horizon (VMS), while the last target occurs in the occurrence area of metaultramafic rocks, where gold mineralization occurrences have not been previously described, being a promising target for future investigations.

Keywords: electrical prospecting; VMS deposits; Digo-Digo formation

1. Introduction

The deposits of volcanogenic massive sulfide (VMS) usually occur as polymetallic massive sulfide (>40%) lenses rich in base (Cu, Zn, Pb) and precious (Au and Ag) metals. VMS is generated from the focused discharge of hot, metal-rich hydrothermal fluids associated with hydrothermal ocean floor convection. For this reason, VMS deposits are generally classified as "Exhalative" deposits. These deposits can also form as either exhaling stratiform or replacement bodies, and commonly have stockwork-type mineralizations associated with the proximal footwall [1].

There is a strong contrast in physical properties between exhalative horizons and their host rocks due to the presence of large chalcopyrite and pyrrhotite amounts [2–4]. Such properties include density, magnetic intensity and susceptibility, gravity, electrical resistance, and acoustical velocity [5]. Due to these different physical properties, gravimetry, self-potential, magnetics, electromagnetics, and induced polarization methods have been successfully used for prospecting VMS deposits [5–20].

Recently, electrical resistivity and induced polarization surveys have been successfully applied to generate polymetallic targets in the Skellefte mineral district, northern Sweden, where more than 80 VMS deposits have already been discovered [11,21]. The efficiency of applying electrical methods to detect VMS mineralization has been previously attested in works where data acquisition was performed above already known buried ore bodies through drilling [7,21].

In Brazil, the records of VMS-type deposits are scarce [22–29], possibly due to the lack of detailed geological mapping and geophysical surveys in areas with geological potential for these deposits to occur.

The objective of this work is to show the efficiency of the induced polarization in the time and frequency domains for differentiating and identifying potentially mineralized zones in exhalites associated with the VMS-type gold in the Digo-Digo Formation, Serra de Santa Rita greenstone belt, Goiás, Brazil.

2. Area Geology

2.1. Crixás-Goiás Domain

The Crixás-Goiás Domain (CGD) [30], formerly the Archean-Paleoproterozoic Terrain of Goiás [31,32], is located in the central–west portion of Goiás, and is part of the Tocantins Province. The province represents a large Brasiliano/Pan-African orogen of the South American Platform formed by a collision between the Amazonian, Paranapanema, and São Francisco/Congo cratons during the Brasiliano Orogeny, which led to the amalgamation of the West Gondwana (Figure 1).
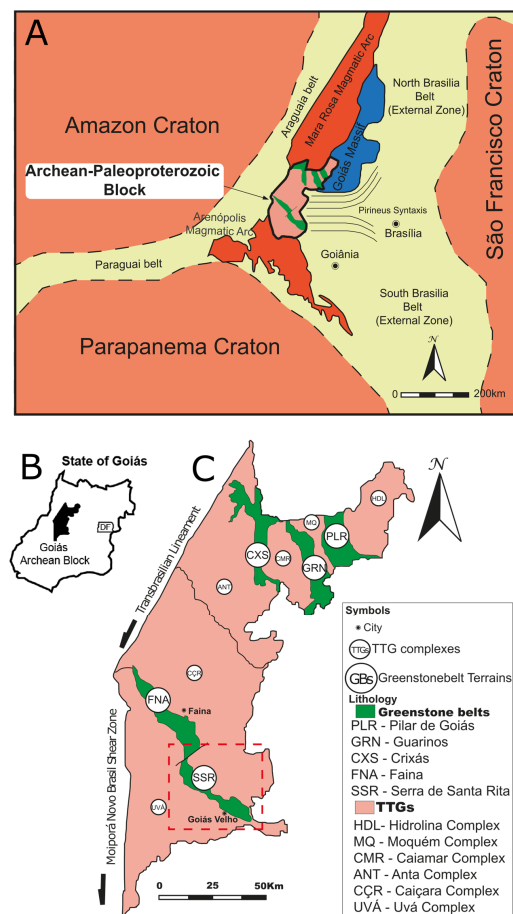

Figure 1. (**A**) Geotectonic scenario and main subdivisions of the Tocantins Province, Central Brazil, emphasizing the Crixás-Goiás Domain in the Brasília Belt (modified from 31). (**B**) Map of Goiás showing the CGD. (**C**) CGD limits and subdivisions; red polygon represents the area of Figure 2 (modified from 35).
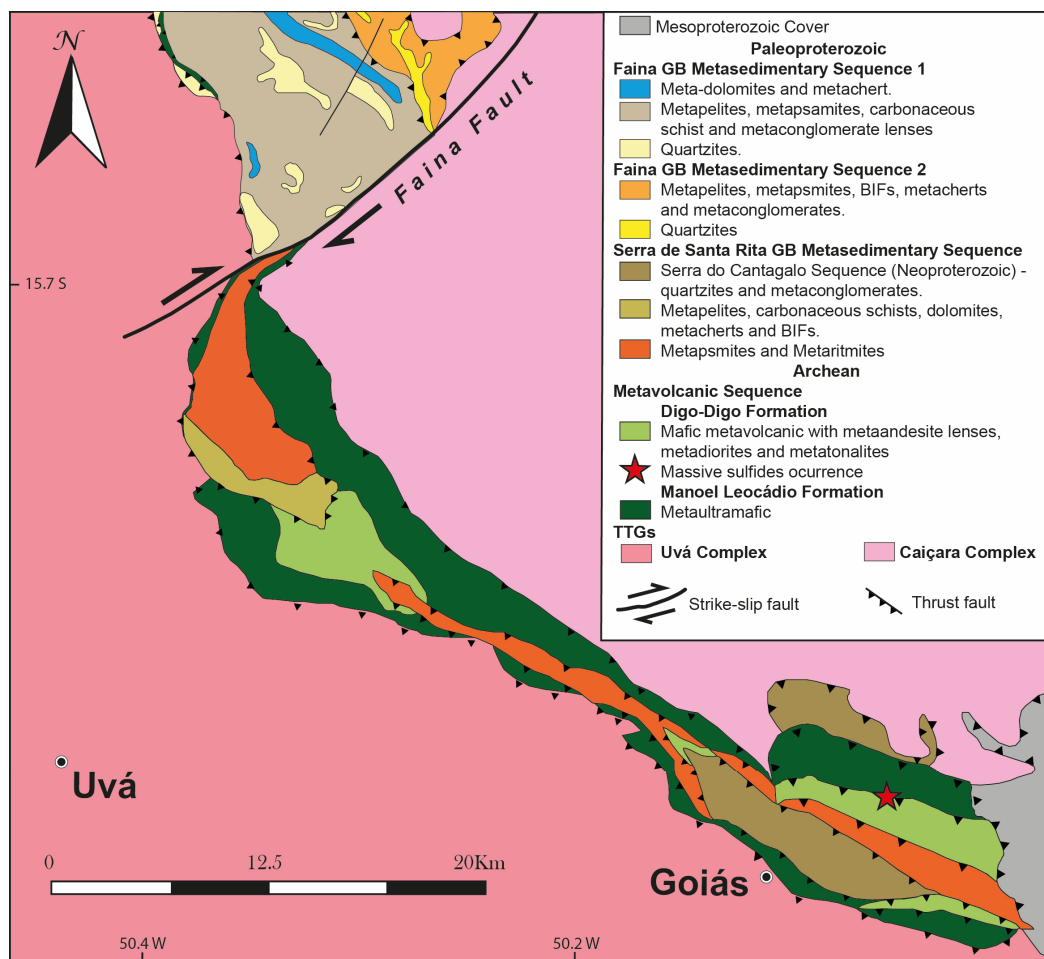
Figure 2. Geological map of the Serra de Santa Rita greenstone belt (modified from 38); the study area corresponds to the massive sulfide occurrence on the map (red star).

The CGD was interpreted as an allochthonous microplate amalgamated on the western margin of the Brasília Belt, in the last evolution stages of the Neoproterozoic orogen [32]. The CGD extends for about 18,000 km^2, consisting of approximately 80% of tonalite–trondhjemite–gneisses-type complexes (TTGs) and 20% of narrow greenstone belts terrains with Archean to Paleoproterozoic ages [33,34].

The granite–gneiss terrains correspond to six main complexes. In the northern portion, Anta, Caiamar, Moquém, and Hidrolina are found, whereas in the south of the block are the Caiçara and Uvá complexes. These complexes have different structural frameworks, ages, and rock associations [35]. The greenstone belts correspond to five narrow and irregular belts. In the north part of CGD are located the greenstone belts of Crixás, Pilar, and Guarinos, while in the south portion are situated the Faina and Serra de Santa Rita greenstone belts.

2.2. Serra de Santa Rita Greenstone Belt

In the southern portion of the Crixás-Goiás Domain, the Faina and Serra de Santa Rita greenstone belts are juxtaposed along an N 30° E dextral fault (Figure 2), extending approximately 100 km in length and up to 7 km in width [36,37]. The two greenstone belts have similar basal sequences, composed of volcanic sequences, but the upper sedimentary records are contrasting and represent different depositional regimes with a probable Paleoproterozoic age [35,36,38,39].

The basal sequence of the Serra de Santa Rita greenstone belt consists of volcanic rocks of ultramafic composition, which characterize the Manoel Leocádio Formation, followed by

mafic and intermediate volcanic rocks of the Digo-Digo Formation [36]. The basal volcanic sequence was dated in 2.96 and 2.92 Ga [38] and covered by a sedimentary sequence formed by carbonaceous phyllites, with intercalations of metachert, calc-shists, banded iron formations, and metagraywacke composing a typical turbiditic sequence [38].

2.3. Digo-Digo Formation

The base of the Digo-Digo Formation consists of mafic metavolcanic rocks represented by amphibole schists with varying proportions of actinolite, albite, epidote, and quartz, intercalated with thin layers of feldspathic metatuffs, talc schists, carbonaceous metapelites, and metacherts [36]. The upper portion of the Digo-Digo Formation consists of sericite–chlorite–quartz schists with relics of original pyroclastic textures ranging from recrystallized ash to coarse tuffs, including abundant layers with lapilli-sized fragments. The composition of the felsic tuffs varies from predominantly dacitic to rhyolitic [36]. The volcanoclastic rock granulometry tends to increase towards metric exhalative horizons composed of metachert banded with carbonaceous phyllite, rich in pyrite and gold (0.5 to 2 ppm), or intervals of massive pyrite [35,40]. U-Pb dating in zircons of andesitic metavolcanic rocks of the Digo-Digo formation indicates an age of 2.97 Ga [41].

2.4. Local Geology

The study area is located at the confluence of Digo-Digo Creek and the Vermelho River, where the upper portion of the Digo-Digo Formation outcrops and massive sulfide layers are exposed. To characterize the main geological units and structures, the area was mapped at a 1:10,000 scale (Figure 3A).
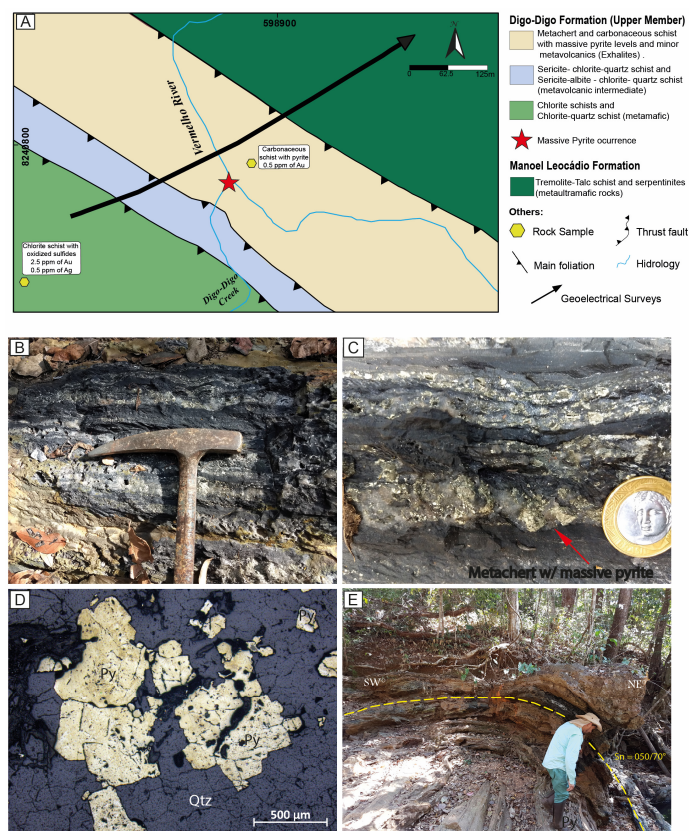
Figure 3. (**A**) Detailed geological map of the confluence region of the Digo-Digo Stream with the Vermelho River. (**B**) Carbonaceous metachert layer with centimetric scale massive sulfides. (**C**) Detail of Figure 3(**B**), with bands/horizons of coarse-grained pyrite. (**D**) Polished section of metachert with pyrite aggregates showing modal composition of 35%–45% pyrite and 45%–55% quartz. (**E**) Carbonaceus metachert layer folded.

In the area, the Digo-Digo Formation is characterized by three distinct stratigraphic units: (i) a mafic metavolcanic unit; (ii) an intermediate metavolcanic unit; and (iii) an exhalative unit (see Figure 3A). The boundaries between these units are delineated by NW-verging thrust faults. Within all these units, the primary tectonic foliation trends in the northwest direction and typically dips between 300 and 700 degrees to the southwest.

The mafic metavolcanic unit outcrops in the southwest portion of the area and comprises mafic schists and amphibolites. The mafic schists consist of varying proportions of chlorite, epidote, actinolite, and hornblende, sometimes with the presence of magnetite, disseminated sulfides, and boxwork textures. The amphibolites are composed of hornblende, plagioclase, ±epidote, ±chlorite, and exhibit tectonic foliation marked by the preferential orientation of hornblende. The metamafic rocks exhibit a transitional geochemical signature, enriched with light rare earth elements and pronounced negative anomalies of Nb and Ti, similar to the patterns of oceanic arc basalts. Additionally, the amphibolites have a high Nb content, showing similarities with Nb-enriched basalts generated in modern subduction zone environments.

The intermediate metavolcanic unit is composed of metandesites, metatuffs, and rare subvolcanic bodies of metadiorite. Typically, discontinuous layers of metandesite are interlayered with metatuffs. In less deformed areas, the metandesites display a porphyritic texture, consisting of euhedral to subhedral phenocrysts of plagioclase (20 to 35%), immersed in a fine matrix (comprising 65 to 80% of the rock) composed of plagioclase, quartz, muscovite, biotite, and chlorite. When intensely deformed, the original texture is entirely obliterated, giving way to pervasive tectonic foliation.

Andesitic metatuffs levels occur intercalated with the metandesites and may represent different episodes of explosive eruption or, alternatively, duplicated and disrupted layers due to later tectonic processes. In less deformed regions, a diagnostic feature of the metatuffs is the high content of plagioclase crystals (70%–80%) surrounded by a fine-grained matrix (20%–30%).

Locally, bodies of diorite occur in association with intermediate and mafic volcanic rocks. U-Pb analyses on zircons from the metadiorite and metandesite indicate crystallization ages of 2.96 and 2.97 Ga [41]. The intermediate metavolcanic rocks exhibit calc-alkaline affinity with geochemical signatures similar to high-silica adakites [41]. The geochemical and isotopic signatures of the mafic and intermediate metavolcanic rocks suggest that the evolution of this supracrustal sequence is linked to the development of a Mesoarchean volcanic arc [38,41].

The exhalative horizon of the Digo-Digo Formation outcrops near the confluence of the Digo-Digo Creek with the Vermelho River. It is represented by intercalations of centimeter- to meter-scale layers of metavolcanics, metacherts, and carbonaceous phyllites. Massive sulfide lenses, with traces of gold, are hosted within this exhalative horizon (Figure 3B,C). Decimeter-scale lenticular levels of metachert are interlayered with chlorite schists. These rocks are generally composed of very fine-grained recrystallized quartz (~30 μm), possibly containing subordinate amounts of chlorite/muscovite and opaque minerals, as well as carbonaceous material. The sulfide lenses are hosted in carbonaceous metachert and comprise 30 to 50% pyrite, 40 to 70% quartz with muscovite and ilmenite as trace minerals.

The main outcrop of the exhalative horizon, which hosts the massive sulfide lenses, is strongly deformed and exhibits metric to decametric tight asymmetrical folds verging towards NE (Figure 3D). Apart from the notable gold content found in rock samples from the massive sulfide lenses, petrographic studies conducted in the exhalative horizons near the Vermelho River confluence have uncovered gold grains exceeding 5 μm in size. These grains are hosted within centimeter-scale sericite–albite–chlorite schists of the intermediate metavolcanic unit [41].

On the northern margin of Vermelho River, the exhalative horizon is in tectonic contact with the metaultramafic rocks of the Manoel Leocádio Formation, primarily represented by talc schists and talc–tremolite schists (Figure 3A).

3. Methodology

3.1. Data Acquisition

The electrical resistivity and chargeability data were acquired over a 550 m section where massive outcropping sulfide layers are exposed. Three sets of data were acquired in the same spatial positions due to the difficult access and crossing of the banks of the Vermelho River (Figure 3A). The SW-NE survey line was positioned perpendicularly to the main direction of the regional geological structures to reduce the effects of three-dimensional structures that cannot be accurately modeled via 2D inversions, thus causing distortions in the electrical resistivity models [29,42–44].

The apparent resistivity and chargeability data were acquired using the Syscal Pro Switch 72 multi-electrode resistor (Iris Instruments, Orléans, France; Figure 4A). Field acquisitions were performed using the time and frequency domain IP methods with dipole–dipole array and 10 m spacing electrodes. In the IP time mode, non-polarizable electrodes were used at the electrical potential recording points and stainless-steel electrodes at the electric current injection points.
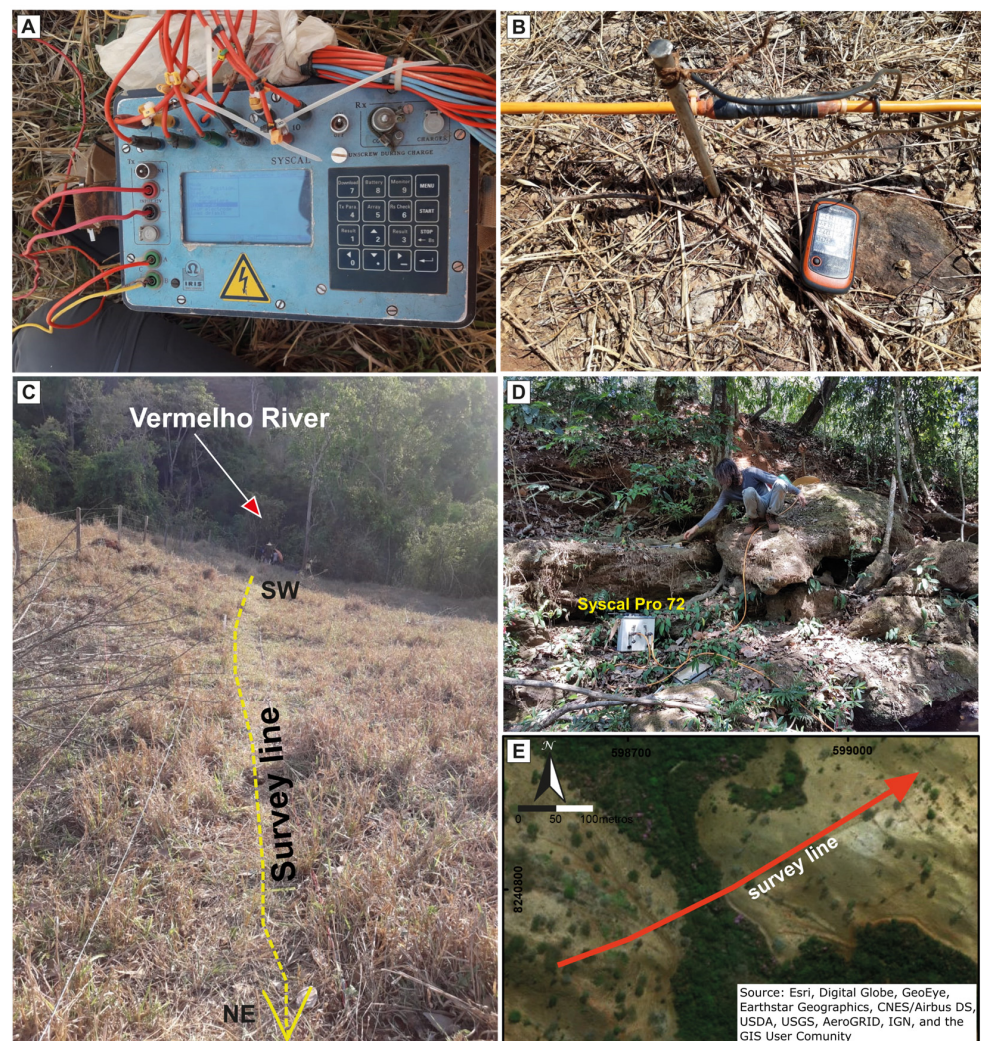

Figure 4. (**A**) Resistivity meter Syscal Pro 72, prepared for acquiring chargeability measurements. (**B**) Stainless steel electrode connected to a multi-cable to perform resistivity measurements (250 and 1000 ms). (**C**) Survey line for measuring chargeability on the northeast bank of the Vermelho River. (**D**) Position of the Syscal Pro during resistivity data (250 and 1000 ms) acquisition on the southwest bank of the Vermelho River. (**E**) Spatial configuration of the electric survey line.

In the IP frequency, 250 and 1000 ms electrical resistivity recording periods were applied, using multi-electrode systems with stainless steel electrodes (Figure 4B). In both surveys, a saline water compound was added to the injection/current record and electrical potential points to reduce the high values of contact resistance.

The survey sections performed with multielectrode systems (250 and 1000 ms) reached 56 m depth, while the resistivity and chargeability (2000 ms) acquisition carried out simultaneously using common cables and porous potential electrodes reached only 32.5 m depth, limited by the maximum of 10 depth investigation levels of the equipment (Figure 4C–E).

3.2. Data Modeling

The electrical resistivity and chargeability data were reduced and filtered separately using the software Prosys 2.0 (Iris Instruments):

Electrical resistivity: (1) conversion to absolute values (the negative records correspond to negative electrical potential measurements that result from a reversal of electrical current); (2) insertion of topography at each electrode point; and (3) filtering of electrical resistivity outliers, high values (spikes), null values (caused by the lack of electrical current that sometimes occurred due to accidental disconnection between the electrodes and cables). Most of the outliers correspond to the Vermelho River passage places and where colluvial sediments (boulders) are present on the surface (Figure 5).
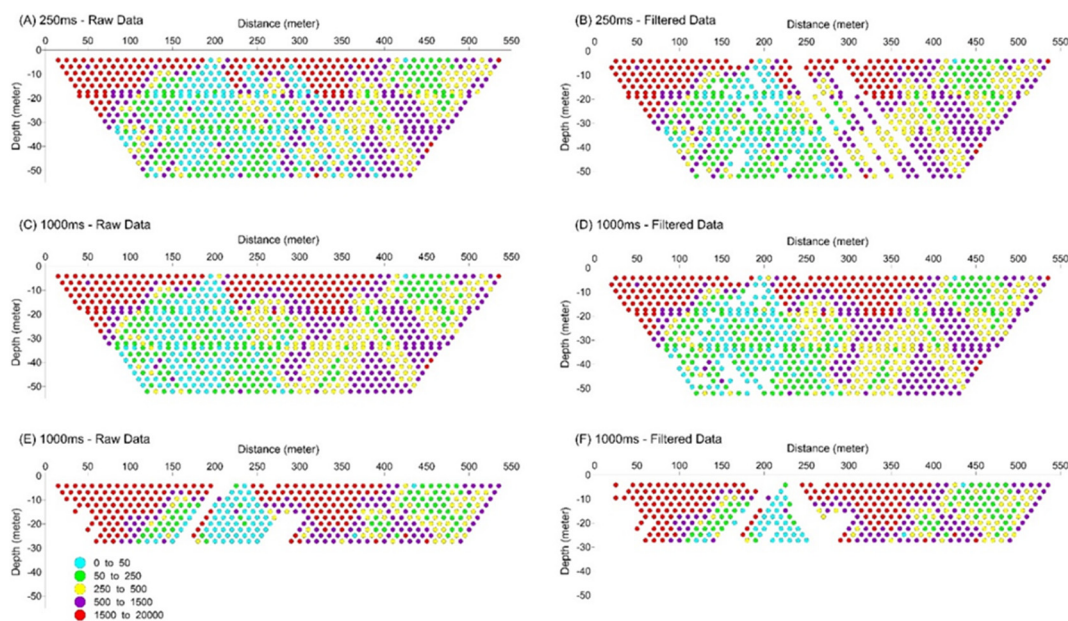

Figure 5. Distribution of the electrical resistivity measurement points in the Digo-Digo Stream region. Sections of raw and filtered data, obtained with sampling periods of 250, 1000, and 2000 ms. (**A**) 250 ms—raw data. (**B**) 250 ms—filtered data. (**C**) 1000 ms—raw data. (**D**) 1000 ms—filtered data. (**E**) 2000 ms—raw data. (**F**) 2000 ms—filtered data.

Chargeability: (1) removal of data where the electric potential decay curves did not follow an exponential behavior, that is, the temporal windows' decay curve behaved erratically without monotonous tendencies with patterns different from the assumed Cole–Cole model; (2) negative or null charge records; and (3) values greater than 100 mV/V so that the decay curve did not present perfect monotonous tendencies. Figure 6 shows the chargeability data recorded in the field (Figure 6A), and after data filtering (Figure 6B). Figure 6C shows the electric potential decay curves of each registered point, and in Figure 6D, these are shown after removing the incoherent curves (without exponential decay).
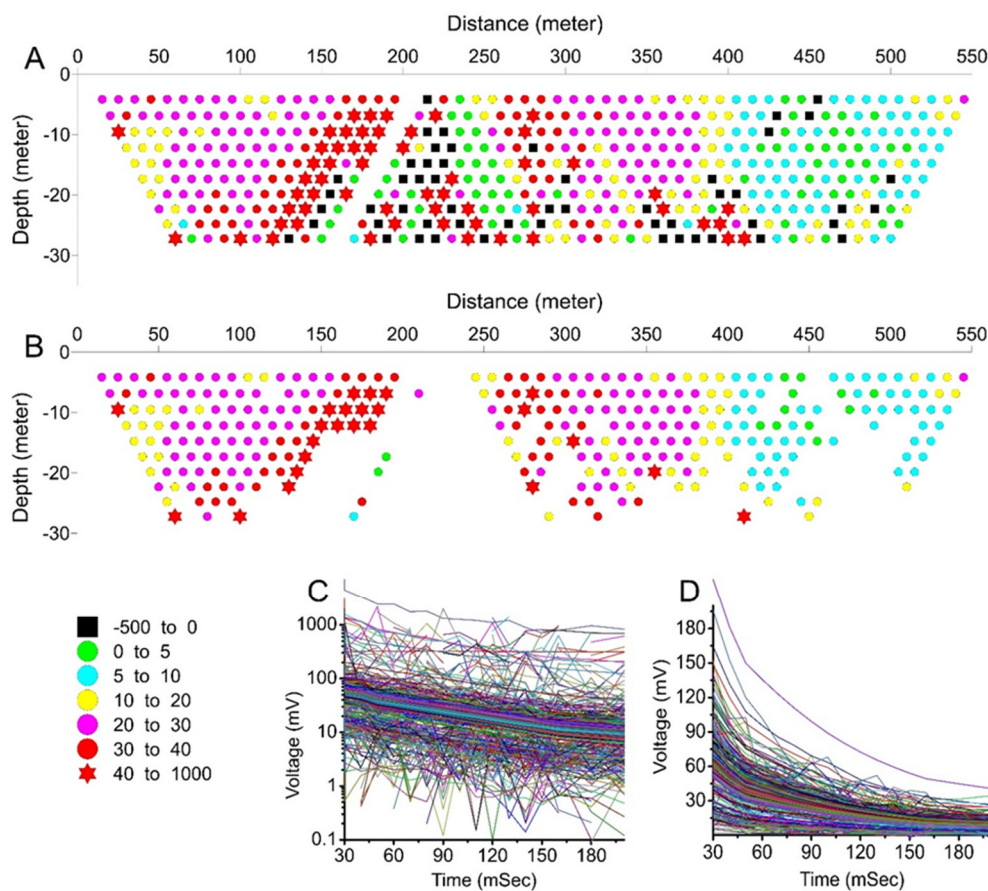
Figure 6. (**A**) Sampling points of chargeability data indicating the lack of sampling only at the Digo-Digo stream crossing—210 m. (**B**) Filtered sampling points. Decay curves of the electrical potential of raw data (**C**) and after filtering (**D**).

After filtering, the inverse modeling of 2D data was performed in the Res2Dinv inversion software [45], which uses least-squares inversion as a standard to minimize the square of the difference between the measured and calculated resistivities. The apparent resistivity data were inserted in the program and filtered for a second time using the exterminate bad datum points tool, followed by the application of the inversion routine.

In the frequency-domain-induced polarization, the apparent resistivity is measured at two different frequencies commonly varying between 0.1 and 10 Hz, while the result is presented as a percentage of effective frequency and/or metal factor [45]. The metal factor (MF) is a standardized parameter used mainly in the frequency-domain-induced polarization method [34]. Despite not measuring any exclusive physical property, this parameter is extensively used in mineral exploration as a data display technique [46]. Based on induced polarization results obtained in the field, ref. [34] suggests that the metal factor is a much better indicator of the mineralization quantity responsible for causing an IP anomaly greater than the frequency effects (PFE). The metal factor can be calculated for both frequency and time domain measurements. In the frequency domain, the metal factor (MF_f) value is calculated as in Equation (1) [45].

$$MF_f = 10^5 \left(\frac{\rho_{dc} - \rho_{ac}}{\rho_{ac}^2} \right) \tag{1}$$

where ρ_{dc} and ρ_{ac} are the resistivity values measured at low and high frequencies, respectively, expressed as ohms per meter. In the time domain, the metal factor is calculated as in Equation (2) [47,48].

$$MF_t = 10^3 \left(\frac{M}{\rho_{ac}} \right) \tag{2}$$

where the chargeability (*M*) is expressed in milliseconds [46].

The metal factor values were also calculated for the unfiltered data (only the topographic correction was performed) using the above equations in module (to avoid negative values). Subsequently, the calculated MF values were filtered to exclude the outliers, points with extremely high Root Mean Square Error (RMS) values.

For metal factor calculations, the topography was initially inserted in the raw data to correct the resistivity values. Subsequently, the MF calculation was performed using module Equation (2) to avoid negative results. Then, outlier MF values or those with exceedingly high RMS errors were eliminated, aiming to reduce the high variance in MF data and consequently reduce the RMS error values of the inversion models.

4. Results

4.1. Electrical Resistivity

Six main geoelectric zones with high lateral contrast are observed in the three electrical resistivity sections (Figure 7) as follows:

i. Thick layer of high resistivity positioned between 0 and 70 m, with values ranging from 1100 to 9000 ohm·m;

ii. Thick layer of low resistivity positioned between 100 and 215 m, with values ranging from 7 to 200 ohm·m underlying a thin superficial layer of high resistivity with values above 7000 ohm·m;

iii. Low resistivity zone position between 215 and 400 m, similar to (ii) but with slightly higher resistivity values ranging from 65 to 500 ohm·m;

iv. Thick zone of low resistivity associated with zones of medium resistivity ranging from 25 to 1000 ohm·m, which is better observed in the 250 ms section (Figure 6C), positioned between 400 and 550 m;

v. Surface zone at the top of the electrical profile with high resistivity, with values above 7000 ohm·m, extending laterally over almost every profile;

vi. Surface zone in lateral contact with zone (v), with low resistivities varying between 30 and 500 ohm·m, occurring between 410 and 480 m on the surface.

4.2. Chargeability

The chargeability model obtained after the inverse modeling converged with 7.5% RMS error after four iterations (Figure 8). In Section 2D, there are three main positive anomalies with values ranging from 45 to 100 mv/V between 100 and 360 m. The three main anomalies identified have a spatial association with zones (ii) and (iii) that have the lowest values of resistivity obtained in the survey on the exhalative horizon of the Digo-Digo Formation. In the IP time section, there is also a vertical anomaly with high chargeability at a depth of 24 m at a position of 400 m. This anomaly correlates with the high resistivity zone (3000 and 8000 ohm).

4.3. Metal Factor

After filtering the data, the metal factor calculated using the models (Figure 8) presented values between 0 and 35,500. Therefore, the RMS error calculated via RES2DINV reaches approximately 80% due to the high variation (1 to 35,500) in the normalized values resulting from the metal factor calculations.
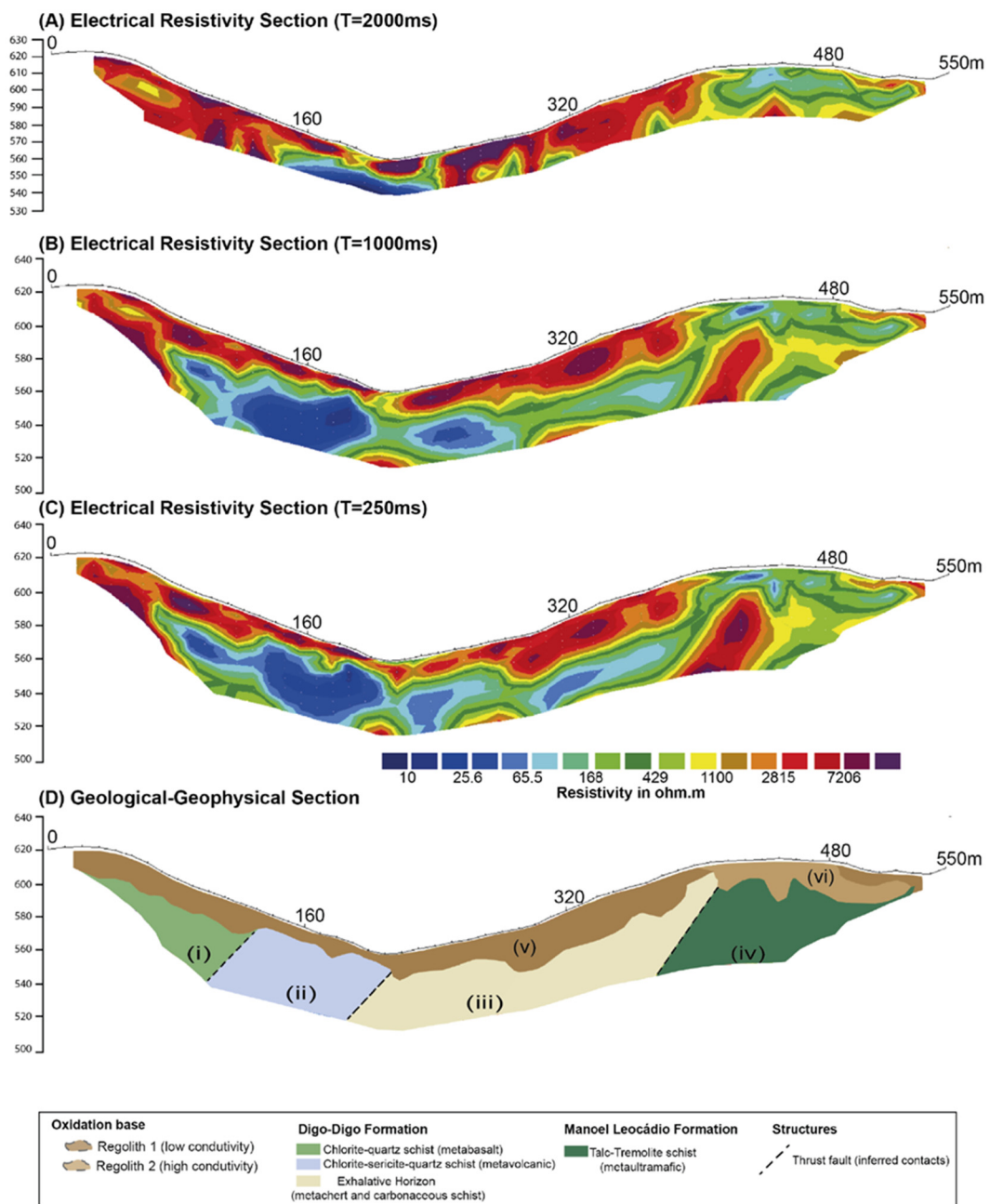
Figure 7. Electrical resistivity models obtained with current cycles of 2000 ms (**A**), 1000 ms (**B**), and 250 ms (**C**). (**D**) Geophysical–geological model of the 2D section elaborated from the correlation of the resistivity data with surface geological data.

The main positive anomalies observed in both metal factor inversions ranged between 20,500 and 35,500 and are spatially associated with the survey central portion, where the main IP anomalies corresponding to low resistivity areas in the electrical resistivity model also occur. In general, the anomalies in the MF models had lower values in the time domain compared to the frequency domain.

The MF time domain model showed three pinnacle-shaped anomalies, with mean values of 25,500 and greater than 30,000 at certain points in time. The MF frequency domain model presented two anomalies with values greater than 30,000, the anomalies continue in the central portion of the data (160–300 m) where values below 10,000 are observed, and the model geometry of the anomalies approximates a slightly distorted arched layer (Figure 8).
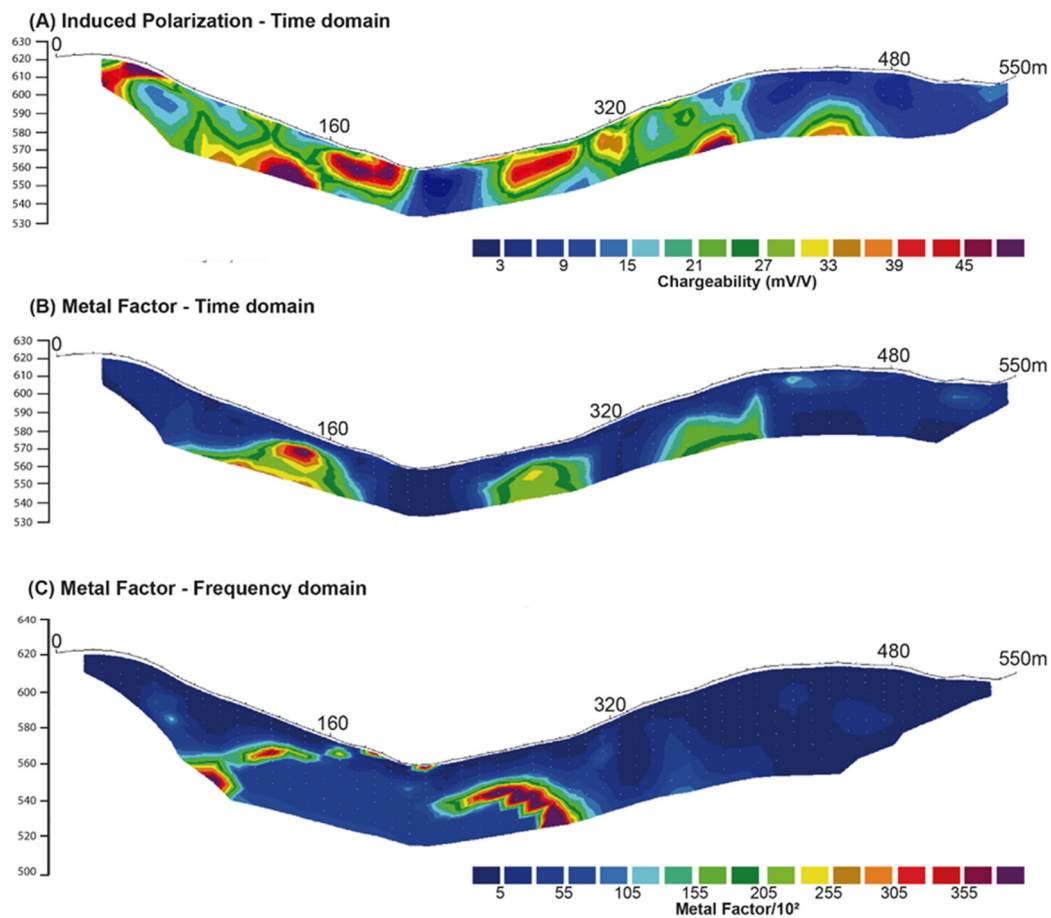
Figure 8. Electrical models: (**A**) chargeability (time domain IP), (**B**) time domain metal factor and (**C**) frequency domain metal factor.

4.4. Data Correlation

To determine the best subsurface locations that can potentially host mineralizations associated with massive and disseminated sulfides, the electric models were imported into the Oasis Montaj 9.1 software to correlate the chargeability, resistivity and metal factor data (frequency domain).

After that, new interpolations were performed via the Inverse Distance Weighting (IDW) method and the results showed acceptable correspondence with the models previously generated in the Res2Dinv software (version 3.71.118). This method assumes that the value attributed to a non-sampled point is the weighted average of the known neighboring values and that the weights between the non-sampled and sampled locations are inversely correlated [49]. The interpolation used cell size values of 2.7 m (approximately 1/2 of the spacing between points), and the values applied to the slope and power variables are, respectively, 1 and 2, which correspond to the software standard values.

Subsequently, the new grids were superimposed on the RGB (red-green-blue) and CMY (cyan-magenta-yellow) spectra, resulting in two ternary models. In these products, the zones with high chargeability as well as high metal factor and conductivity (low resistivity) are superimposed, highlighting the areas with the greatest potential for mineralization associated with the presence of metal sulfides.

In the ternary models (Figure 9), the purple colors in the RGB spectrum and greenish in the CMY indicate areas with greater potential for mineralization occurrence, while areas colored green (RGB) and purple/pink (CMY) suggest areas of high resistivity and low metal factor and chargeability values, indicating zones with properties of non-metallic materials and possible barren zones.
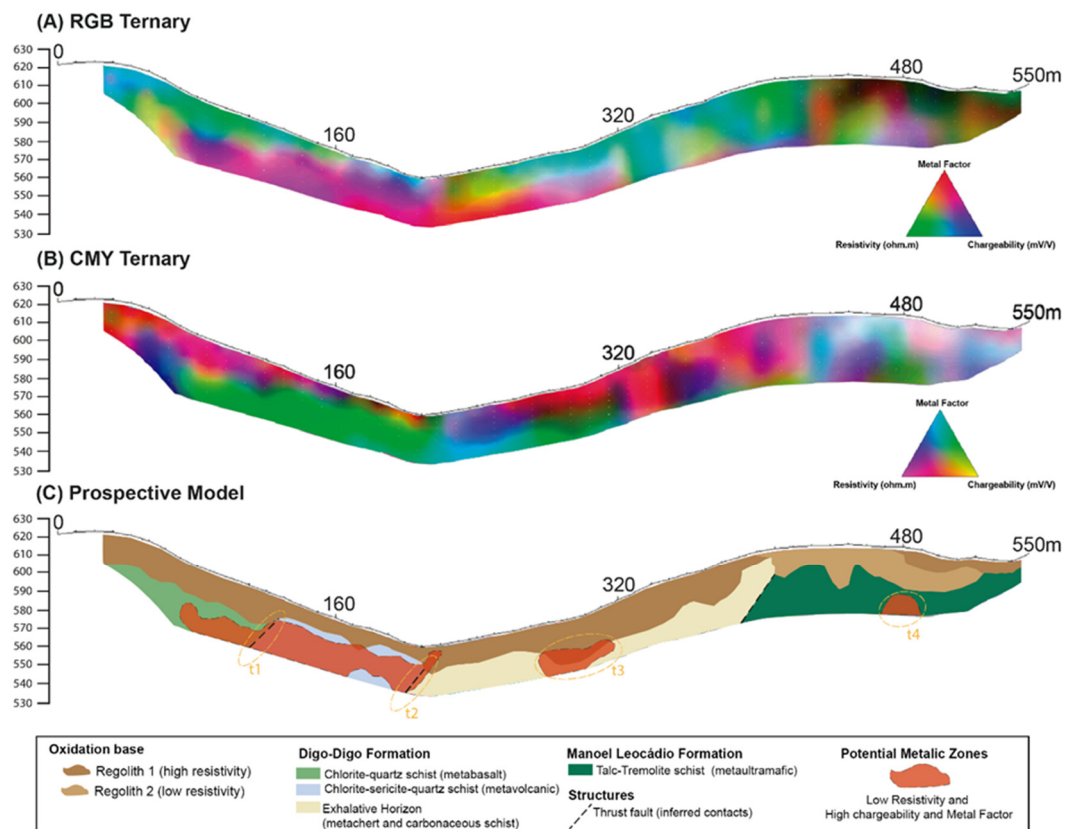
Figure 9. Ternary models resulting from the integration of 2D results of electrical resistivity, charge-ability and metal factor (frequency domain). (**A**) Electric ternary (RGB); areas with greater potential to host metallic minerals are colored purple and pink. (**B**) Electric ternary (CMY); an area with high potential for mineralization is colored green. (**C**) Prospective model for the confluence region of the Digo-Digo stream with Vermelho River; areas with high potential to host metallic minerals are highlighted in red. More restricted target areas (t1, t2, t3 and t4) are identified by orange circles.

In ternaries, three zones with the characteristics with potential for sulfide mineralization occur between (1) 75 and 220 m, (2) 270 and 310 m, and (3) 470 and 490 m, starting at depths between 10 and 20 m (Figure 9).

5. Discussion and Conclusions

The geological information obtained on the surface is consistent with the respective lateral variations identified in the electrical resistivity sections.

i. Zone (i) is spatially associated with chlorite–quartz schists from the Digo-Digo Formation;
ii. Zone (ii) correlates spatially with intermediate metavolcanic rocks (sericite–chlorite–quartz schists);
iii. Zone (iii) refers to the central areas of the survey, has the lowest resistivity values of the section, and can be spatially correlated to the exhalative horizon with disseminated to massive levels of pyrite and gold traces.
iv. Zone (iv) occurs to the northeast portion of the Vermelho River, with different electrical responses and intermediate resistivity values (500–1100 ohms.m) and spatial correlation with the meta-ultrabasic rocks of the Manoel Leocádio Formation.
v. The zones (v) and (vi) of the model correspond to two superficial layers (top of the profiles) with different resistivity values; zone (v) corresponds to a layer with resistivity values between 5000 and 8000 ohms.m that extends laterally over almost the entire profile, except between 400 and 480 m. These zones are interpreted as a product of rock weathering (regolith).

vi.   Based on the electrical characteristics of the zones (i to vi), the geological data obtained on the surface, and their correlations, we propose an interpreted section with lithologies, structures, and coverage of the electrical resistivity models.

The model integrating the electrical resistivity, chargeability and metal factor (frequency domain) data generated by superimposing the models in the RGB and CMY spectra enables the determination of the zones with higher potential to host mineralizations associated with sulfides and, finally, the proposal of a prospective model of the studied section.

From the prospective model and the areas with potential for mineralization, four prospective targets were generated (t1, t2, t3 and t4):

- Targets t1 and t2 correspond to possible contact zones with the possible presence of metallic minerals; t1 is at the contact of chlorite–quartz schists (metabasalts) with the intermediate metavolcanic rocks, and t2 at the contact between the intermediate metavolcanic with the exhalative horizon; deposits and mineral occurrences are commonly associated with geological contact zones due to metal remobilizations, structural controls (shear zones), redox reactions and differences in buffering or permeability between rocks [50].
- The t3 target is hosted in the intercalations of metavolcanic, metacherts and carbonaceous phyllites with disseminated to massive sulfide levels containing gold traces, the target of the present study.
- Target t4 is hosted in the metaultramafic rocks of the Manoel Leocádio Formation, where previous studies described no associated mineralization; therefore, this target region has been selected for further investigation.

Some geological structures, such as the possible folding evidenced in the exposure of rocks from the exhalative horizon, could not be clearly identified in the resistivity and chargeability data due to the resolution of the acquired data. However, the MF frequency domain model shows that the zone with anomalous metal factor values presents a continuous geometry similar to the shape of an open fold of hectametric scale. If the geometry present in the MF model really corresponds to a geological structure, the fold observed in the field might be a parasitic fold that can be associated with a larger scale fold of the metal factor model.

Regarding the differences identified in the acquired data and results in the time and frequency domains, the following can be observed:

(1)   The frequency domain IP data acquired using multi-electrodic systems obtained electrical resistivity measurements in 80% more points, reaching about 20 m deeper than in the time domain, and required only 50% of the acquisition time.

(2)   The chargeability data had broader and more dispersed anomalies across the section, while the frequency domain metal factor data showed more restricted and structured anomalies, but still with good spatial correlation with chargeability and time domain metal factor data, mainly in the central portion associated with the exhalative horizon of the Digo-Digo Formation.

In conclusion, in cases of exploration projects that require data acquisition with greater depths and reduced costs, the frequency domain method using electrical resistivity meters with relatively low current transmissions was proven to be as efficient as the time domain data for detecting potential mineralized zones in the Digo-Digo Formation.

Author Contributions: Conceptualization, W.R.B., C.L.B.T. and P.A.C.d.A.; methodology, W.R.B. and P.A.C.d.A.; software, P.A.C.d.A. and W.R.B.; validation, P.A.C.d.A., W.R.B. and A.M.S.; formal analysis, W.R.B., P.A.C.d.A. and C.L.B.T.; investigation, W.R.B., P.A.C.d.A., C.L.B.T., A.M.S. and H.V.d.G.; writing—original draft preparation, P.A.C.d.A., W.R.B., C.L.B.T. and M.H.L.S.; writing—review and editing, P.A.C.d.A., W.R.B., C.L.B.T., A.M.S. and M.H.L.S.; visualization, W.R.B., P.A.C.d.A., C.L.B.T. and M.H.L.S.; supervision, W.R.B. and C.L.B.T.; project administration, C.L.B.T., A.M.S. and W.R.B. All authors have read and agreed to the published version of the manuscript.

References

1. Galley, A.G.; Hannington, M.D.; Jonasson, I.R. Volcanogenic massive sulfide deposits. In *Mineral Deposits of Canada: A Synthesis of Major Deposit-Types, District Metallogeny, the Evolution of Geological Provinces, and Exploration Methods*; Special Publication; Geological Association of Canada, Mineral Deposits Division: Ottawa, ON, Canada, 2007; Volume 5, pp. 141–161.
2. Pelton, W.H.; Ward, S.H.; Hallof, P.G.; Sill, W.R.; Nelson, P.H. Mineral discrimination and removal of inductive coupling with multifrequency IP. *Geophysics* **1978**, *43*, 588–609. [CrossRef]
3. Palacky, G. Resistivity Characteristics of Geological Targets. In *Electromagnetic Methods in Applied Geophysics-Theory*; Nabighian, M., Ed.; Society of Exploration Geophysicists: Tulsa, OK, USA, 1987; pp. 53–129.
4. Clark, D.A.; Emerson, D.W.; Kerr, T.L. The use of electrical conductivity and magnetic susceptibility tensors in rock fabric studies. *Explor. Geophys.* **1988**, *19*, 244. [CrossRef]
5. Morgan, L.A. Geophysical Characteristics of Volcanogenic Massive Sulfide Deposits. In *Volcanogenic Massive Sulfide Occurrence Model*; Shanks, P., Thurston, R., Eds.; US Geological Survey: Reston, VA, USA, 2012; pp. 113–131.
6. Paterson, N.R.; Hallof, P.G. *Geophysical Exploration for Gold. Gold Metallogeny and Exploration*; Springer: Boston, MA, USA, 1993. [CrossRef]
7. Dentith, M.C.; Frankcombe, K.F.; Trench, A. Geophysical signatures of Western Australian mineral deposits: An overview. *Explor. Geophys.* **1994**, *25*, 103. [CrossRef]
8. McIntosh, S.M.; Gill, J.P.; Mountford, A.J. The geophysical response of the Las Cruces massive sulfide deposit. *Explor. Geophys.* **1999**, *30*, 123. [CrossRef]
9. Swiridiuk, P.; Close, B. Geophysical surveying over VMS deposits in Oman. *ASEG Ext. Abstr.* **2004**, 1–4. [CrossRef]
10. Hodges, G.; Chen, T.; Van Buren, R. HELITEM detects the Lalor VMS deposit. *Explor. Geophys.* **2016**, *47*, 285–289. [CrossRef]
11. Tavakoli, S.; Dehghannejad, M.; Juanatey, M.A.G.; Bauer, T.; Weihed, P.; Elming, S. Potential Field, Geoelectrical and Reflection Seismic Investigations for Massive Sulfide Exploration in the Skellefte Mining District, Northern Sweden. *Acta Geophys.* **2016**, *64*, 2171–2199. [CrossRef]
12. Newton, O.; Vowles, A. Geophysical Overview of Lalor VMS Deposit. In Proceedings of the Exploration 17: Sixth Decennial International Conference on Mineral Exploration, Toronto, ON, Canada, 21–25 October 2017; Tschirhart, V., Thomas, M.D., Eds.; Canadian Science Publishing: Ottawa, ON, Canada, 2017; pp. 619–635.
13. Ugalde, H.; Morris, W.A.; Van Staal, C. The Bathurst Mining Camp, New Brunswick: Data Integration, Geophysical Modelling and Implications for Exploration. *Can. J. Earth Sci.* **2018**, *56*, 433–451. [CrossRef]
14. Palacky, G.J.; Kadekaru, K. Effect of tropical weathering on electrical and electromagnetic measurements. *Geophysics* **1979**, *44*, 69–88. [CrossRef]
15. Claprood, M.; Chouteau, M.; Cheng, L.Z. Rapid detection and classification of airborne time-domain electromagnetic anomalies using weighted multi-linear regression. *Explor. Geophys.* **2008**, *39*, 164. [CrossRef]
16. Cox, L.H.; Wilson, G.A.; Zhdanov, M.S. 3D inversion of airborne electromagnetic data. *Geophysics* **2012**, *77*, WB59–WB69. [CrossRef]
17. Legault, J.M.; Plastow, G.; Zhao, S.; Bournas, N.; Prikhodko, A.; Orta, M. ZTEM and VTEM airborne EM and magnetic results over the Lalor copper-gold volcanogenic massive sulfide deposit region, near Snow Lake, Manitoba. *Interpretation* **2015**, *3*, SL83–SL94. [CrossRef]
18. Gibson, H.L.; Allen, R.L.; Riverin, G.; Lane, T.E. The VMS model: Advances and application to exploration targeting. In Proceedings of the Exploration 07: Fifth Decennial International Conference on Mineral Exploration, Toronto, ON, Canada, 9–12 September 2007; pp. 713–730.
19. Phillips, N.; Oldenburg, D.; Chen, J.; Li, Y.; Routh, P. Cost effectiveness of geophysical inversions in mineral exploration: Applications at San Nicolas. *Lead. Edge* **2001**, *20*, 1351–1360. [CrossRef]
20. Boszczuk, P.; Cheng, L.Z.; Hammouche, H.; Roy, P.; Lacroix, S.; Cheilletz, A. A 3D gravity data interpretation of the Matagami mining camp, Abitibi Subprovince, Superior Province, Québec, Canada: Application to VMS deposit exploration. *J. Appl. Geophys.* **2011**, *75*, 77–86. [CrossRef]

21. Tavakoli, S.; Bauer, T.E.; Rasmussen, T.M.; Weihed, P.; Elming, S. Deep massive sulfide exploration using 2D and 3D geoelectrical and induced polarization data in Skellefte mining district, northern Sweden. *Geophys. Prospect.* **2016**, *64*, 1602–1619. [CrossRef]
22. Araujo, S.M.; Fawcett, J.J.; Scott, S.D. Metamorphism of hydrothermally altered rocks in a volcanogenic massive sulfide deposit: The Palmeirópolis, Brazil, example. *Rev. Bras. Geociências* **1995**, *25*, 173–184. [CrossRef]
23. Neder, R.D.; Figueiredo, B.R.; Beaudry, C.; Collins, C.; Leite, J.A.D. The Expedito Massive Sulfide Deposit, Mato Grosso. *Rev. Bras. Geol.* **2000**, *30*, 222–225. [CrossRef]
24. Hartmann, L.A.; Delgado, I. Cratons and orogenic belts of the Brazilian Shield and their contained gold deposits. *Miner. Depos.* **2001**, *36*, 207–217. [CrossRef]
25. NetunoVillas, R.; Santos, M. Gold deposits of the Carajás mineral province: Deposit types and metallogenesis. *Miner. Depos.* **2001**, *36*, 300–331. [CrossRef]
26. Grainger, C.J.; Groves, D.I.; Tallarico, F.H.B.; Fletcher, I.R. Metallogenesis of the Carajás Mineral Province, Southern Amazon Craton, Brazil: Varying styles of Archean through Paleoproterozoic to Neoproterozoic base- and precious-metal mineralization. *Ore Geol. Rev.* **2008**, *33*, 451–489. [CrossRef]
27. Fruchting, A.; Boniatti, J.; Oliveira, G.; Oliveira, S.B.; Pires, P.F.R.; Henrique, E. Aplicação dos métodos eletromagnéticos aéreos e de polarização induzida espectral em mineralizações de cobre/zinco tipo VMS. In Proceedings of the 11th International Congress of the Brazilian Geophysical Society & EXPOGEF 2009, Bahia, Brazil, 24–28 August 2009. [CrossRef]
28. Teixeira, J.B.G.; Silva, M.G.; Misi, A.; Cruz, S.C.P.; Silva Sá, J.H. Geotectonic setting and metallogeny of the northern São Francisco craton, Bahia, Brazil. *J. S. Am. Earth Sci.* **2010**, *30*, 71–83. [CrossRef]
29. Couto, M.A., Jr.; Wosniak, R.; Marques, E.D.; Duque, T.; Carvalho, M.T.N. VTEM and Aeromagnetic Data Modeling Applied to Cu, Zn and Pb Prospection in Palmeirópolis Project, TO, Brazil. In Proceedings of the 15th International Congress of the Brazilian Geophysical Society, Rio de Janeiro, Brazil, 31 July–3 August 2017. [CrossRef]
30. Cordeiro, P.F.O.; Oliveira, C.G. The Goiás Massif: Implications for a pre-Columbia 2.2–2.0 Ga continent-wide amalgamation cycle in central Brazil. *Precambr. Res.* **2017**, *298*, 403–420. [CrossRef]
31. Jost, H.; Junior, F.C.; Fuck, R.A.; Dussin, I.A. Uvá complex, the oldest orthogneisses of the Archean-Paleoproterozoic terrane of central Brazil. *J. S. Am. Earth Sci.* **2013**, *47*, 201–212. [CrossRef]
32. Pimentel, M.M. The tectonic evolution of the Neoproterozoic Brasília Belt, central Brazil: A geochronological and isotopic approach. *Braz. J. Geol.* **2016**, *46*, 67–82. [CrossRef]
33. Jost, H.; Sial, A.N.; Benell, M.R.; Ferreira, V.P. *Carbon Isotopes in Dolostones of Goias State Greenstone Belts, Central Brazil*; Brazilian Geological Congress: Curitiba, Brazil, 2008; Volume 44, p. 687.
34. Jost, H.; Chemale, F., Jr.; Dussin, I.A.; Tassinari, C.C.G.; Martins, R. U-Pb zircon Paleoproterozoic age for the metasedimentary host rocks and gold mineralization of the Crixás greenstone belt, Goiás, Central Brazil. *Ore Geol. Rev.* **2010**, *37*, 127–139. [CrossRef]
35. Jost, H.; Carvalho, M.J.; Rodrigues, V.G.; Martins, R. Metalogênese dos greenstone belts de Goiás. In *Metalogênese das Províncias Tectônicas Brasileiras*; CPRM: Belo Horizonte, Brazil, 2014; pp. 141–168.
36. Resende, M.G.; Jost, H.; Osborne, G.A.; Mol, A.G. The stratigraphy of the Goiás and Faina Greenstone Belts, Central Brazil: A new proposal. *Rev. Bras. Geociências* **1998**, *28*, 77–94. [CrossRef]
37. Resende, M.G.; Jost, H.; Lima, B.E.M.; Teixeira, A.D.A. Proveniência e Idades modelos Sm/Nd das Rochas Siliciclásticas Arqueanas dos Greenstone Belts de Faina e Santa Rita, Goiás. *Rev. Bras. Geociências* **1999**, *29*, 281–290.
38. Borges, C.C.A.; Toledo, C.L.B.; Silva, A.M.; Junior, F.C.; Jost, H.; de Carvalho Lana, C. Geochemistry and isotopic signatures of metavolcanic and metaplutonic rocks of the Faina and Serra de Santa Rita greenstone belts, Central Brazil: Evidence for a Mesoarchean intraoceanic arc. *Precambrian Res.* **2017**, *292*, 350–377. [CrossRef]
39. Bogossian, J.; Hagemann, S.G.; Rodrigues, V.G.; Lobato, L.M.; Roberts, M. Hydrothermal alteration and mineralization in the Faina greenstone belt: Evidence from the Cascavel and Sertão orogenic gold deposits. *Ore Geol. Rev.* **2020**, *119*, 103293. [CrossRef]
40. Tomazzoli, E.R. Geologia, Petrologia, Deformação e Potencial Aurífero do Greenstone Belt de Goiás-GO. Master's Thesis, Universidade de Brasília, Brasília, Brazil, 1985; 206p.
41. Godoy, H.V. Petrografia e Geoquímica das Rochas Vulcânicas e Sedimentares da Formação Digo-Digo: Implicações Para Prospecção de Depósitos de Sulfetos Maciços Vulcanogênicos no Greenstone belt Serra de Santa Rita, GO. Master's Thesis, Universidade de Brasília, Brasília, Brazil, 2019; 70p. Available online: https://repositorio.unb.br/handle/10482/40498 (accessed on 18 November 2022).
42. Chambers, J.; Ogilvy, R.; Kuras, O.; Cripps, J.; Meldrum, P. 3D electrical imaging of known targets at a controlled environmental test site. *Environ. Geol.* **2002**, *41*, 690–704. [CrossRef]
43. Bentley, L.; Gharibi, M. Two-and three-dimensional electrical resistivity imaging at a heterogeneous remediation site. *Geophysics* **2004**, *69*, 674–680. [CrossRef]
44. Nimmer, R.E.; Osiensky, J.L.; Binley, A.M.; Williams, B.C. Three-dimensional effects causing artifacts in two-dimensional, cross-borehole, electrical imaging. *J. Hydrol.* **2008**, *359*, 59–70. [CrossRef]
45. Loke, M.H. *RES2DINVx64*, Version 4.09. Rapid 2D Resistivity & IP Inversion Using the Least-Square Method-Geoelectrical Imaging 2-D & 3D. Geotomo Software: Penang, Malaysia, 2019; 137p. Available online: https://www.geotomosoft.com/downloads.php (accessed on 18 November 2022).

46. Witherly, K.E.; Vyselaar, J. A Geophysical Case History of the Poplar Lake Copper-Molybdenum Deposit, Houston Area, British Columbia. In *Induced Polarization. Applications and Case Histories*; Ward, S.H., Ed.; Society of Exploration Geophysicists: Tulsa, OK, USA, 1990; pp. 304–324.

47. Madden, T.R.; Marshall, D.J. Induced polarization, a study of its causes. *Geophysics* **1959**, *24*, 790–816. [CrossRef]

48. Telford, W.M.; Geldart, L.P.; Sheriff, R.E. *Applied Geophysics*; Cambridge University Press: Cambridge, UK, 1990; 740p.

49. Lu, G.Y.; Wong, D.W. An adaptive inverse-distance weighting spatial interpolation technique. *Comput. Geosci.* **2008**, *34*, 1044–1055. [CrossRef]

50. Volkov, A.V. Types of Ore Material Remobilization. *Dokl. Earth Sci.* **2005**, *403*, 688–691.